Published in final edited form as:
Ann Biomed Eng. 2008 October ; 36(10): 1690–1698. doi:10.1007/s10439-008-9546-4.

Simulated Two-Dimensional Red Blood Cell Motion, Deformation, and Partitioning in Microvessel Bifurcations

Jared O. Barber[1], **Jonathan P. Alberding**[2], **Juan M. Restrepo**[3], and **Timothy W. Secomb**[4]

1 *Program in Applied Mathematics, University of Arizona, Tucson, AZ 85721, USA*

2 *Arizona Research Laboratories, University of Arizona, Tucson, AZ 85721, USA*

3 *Department of Mathematics and Department of Physics, University of Arizona, Tucson, AZ 85721, USA*

4 *Department of Physiology, University of Arizona, Tucson, AZ 85724, USA*

Abstract

Movement, deformation, and partitioning of mammalian red blood cells (RBCs) in diverging microvessel bifurcations are simulated using a two-dimensional, flexible-particle model. A set of viscoelastic elements represents the RBC membrane and the cytoplasm. Motion of isolated cells is considered, neglecting cell-to-cell interactions. Center-of-mass trajectories deviate from background flow streamlines due to migration of flexible cells towards the mother vessel centerline upstream of the bifurcation and due to flow perturbations caused by cell obstruction in the neighborhood of the bifurcation. RBC partitioning in the bifurcation is predicted by determining the RBC fraction entering each branch, for a given partition of total flow and for a given upstream distribution of RBCs. Typically, RBCs preferentially enter the higher-flow branch, leading to unequal discharge hematocrits in the downstream branches. This effect is increased by migration toward the centerline but decreased by the effects of obstruction. It is stronger for flexible cells than for rigid circular particles of corresponding size, and decreases with increasing parent vessel diameter. For unequally-sized daughter vessels, partitioning is asymmetric, with RBCs tending to enter the smaller vessel. Partitioning is not significantly affected by branching angles. Model predictions are consistent with previous experimental results.

Keywords

microvessel; bifurcation; erythrocyte mechanics; capillary flow; phase separation

INTRODUCTION

Nonuniform partitioning of hematocrit at diverging vessel bifurcations is responsible for the heterogeneous discharge hematocrit distribution that is seen in the microvasculature[17]. Nonuniform hematocrit distribution, in turn, affects the microvascular oxygen distribution, the effective viscosity of blood in microvessels[15], and the distribution of other metabolites. To aid understanding and quantification of microvascular transport in normal and disease states, a more thorough understanding of RBC partitioning in diverging microvascular bifurcations is desirable.

Corresponding author: J.O. Barber, Program in Applied Mathematics, University of Arizona, Tucson, AZ 85721, USA. Tel: (520) 621-2138; Fax: (520) 626-5048; E-mail: jbarber@math.arizona.edu..

Schmid-Schönbein et al.[17] performed some of the earliest experiments that quantified RBC partitioning. Blood flow was filmed in nine rabbit ear capillary bifurcations (diameters ~ 5-15 μm) while the bulk blood flow through the daughter branches was changed by pressing on veins near the bifurcations. Functions were presented that gave the dependence of the approximate fractions of RBC flux in the two daughter branches ($\Phi_{1,2}$) on the fractions of bulk blood flux into those branches ($\psi_{1,2}$) for three bifurcations. The results suggested that the upstream hematocrit distribution at a small diverging bifurcation plays a significant role in RBC partitioning.

Pries et al.[11] observed sixty-five arteriolar bifurcations (diameters ~ 10-30 μm) in rat mesentery, with average discharge hematocrit 20% to 55%. They identified several important parameters that affect the fraction of RBC flux entering a branch: the fraction of bulk blood flux entering that branch, the ratio of the two daughter vessel diameters, the size of the mother vessel, and the upstream hematocrit distribution. They also constructed a function of those parameters that gives an estimate of the RBC flux into the two daughter branches of a bifurcation. This function was later adjusted[14] to give reasonable results for extreme hematocrit and vessel diameter ratios. This adjusted function is used here for comparisons.

Enden and Popel[4] used numerical methods to approximate the Stokes flow in a bifurcating geometry. Assuming that RBC trajectories coincide with fluid streamlines, they produced results consistent with the Pries et al.[11] experiments, for large vessel diameters (25 μm)[5]. However, Audet and Olbricht[2] showed that in small vessels, circular particles with diameters comparable to the vessel diameter could experience significant drift across background fluid streamlines. Similarly, Secomb and El-Kareh[3] found that spherical caps approaching a cylinder (representing the flow divider of a bifurcation) can drift across fluid streamlines. Particle deformability can lead to lateral drift of particles in shear flows[9]. These studies illustrate a need to examine this potential drift if a more accurate understanding of RBC partitioning in small vessels is to be obtained.

Here, a computational model of flexible two-dimensional RBCs[18] is used to identify the mechanical effects underlying the tendency of RBCs to drift, or migrate, across underlying fluid streamlines in small vessel bifurcations (6-13 μm). Effects of particle deformability are examined by comparing the results with those obtained in corresponding simulations using rigid particles. The results are used to predict RBC partitioning in small vessel bifurcations and its dependence on mother vessel size, ratio of daughter diameters, daughter branching angles, and cell deformability.

METHODS

The model describes the motion of a cell in a surrounding Stokes flow as it moves in a rigid vessel in two dimensions. The constraint of constant cell volume that would apply in the three-dimensional case is represented by an effective internal pressure[18]. A single cell in a bifurcation is considered and effects of cell-to-cell interactions are excluded. Nodes are located along the perimeter of the RBC, with an additional internal node, as shown in Fig. 1a. The outer line segments (external elements) are viscoelastic, and represent a planar cross-section of a RBC membrane that possesses shear elasticity, bending elasticity, and in-plane viscosity. The segments connecting the central node to the outer nodes (internal elements) are viscous and are included to represent cytoplasmic and out-of-plane membrane deformation[18].

The outer nodes are numbered from 1 to n and the i^{th} node has coordinates $\mathbf{x}_i = (x_i, y_i)$. The central node has coordinates $\mathbf{x}_0 = (x_0, y_0)$. An external element and the quantities associated with it are denoted by i when the element's endpoints are (x_i, y_i) and (x_{i+1}, y_{i+1}). The i^{th} internal element has as its endpoints (x_0, y_0) and (x_i, y_i).

The average tension in external element i is given by

$$\bar{t}_i = k_t\,(l_i/l_0 - 1) + \mu_m \frac{1}{l_i}\frac{\mathrm{d}l_i}{\mathrm{d}t}, \tag{1}$$

where l_i is the length of the i^{th} external element, $l_0 = 0.97\ \mu$m is a reference length, $k_t = 0.012$ dyn/cm is the elastic modulus, and $\mu_m = 2\times10^{-4}$ dyn s/cm is the viscosity of the external elements[18]. The bending moment acting on the i^{th} node (x_i,y_i) is

$$m_i = -k_b\alpha_i/l_0. \tag{2}$$

Here $k_b = 9\times10^{-12}$ dyn cm is the bending modulus at the nodes[18] and α_i is the angle between two consecutive external elements (Fig. 1a). The factor l_0 converts α_i to a curvature. The internal elements are assumed to have viscous resistance to changes in length,

$$T_i = \mu'_m \frac{1}{L_i}\frac{\mathrm{d}L_i}{\mathrm{d}t}, \tag{3}$$

where L_i is the length of the i^{th} internal element, $\mu'_m = 1\times10^{-4}$ dyn s/cm is the viscosity of the internal elements[18] and T_i is the tension in internal element i.

The fluid inside of the cell is assumed to exert a constant internal pressure on the membrane,

$$p_{int} = k_p\left(1 - A/A_{ref}\right), \tag{4}$$

where A is the area of the cell cross-section, $A_{ref} = 22.2\ \mu\text{m}^2$ is a reference area and $k_p = 50$ dyn/cm^2. RBC volume preservation and surface area preservation lead to approximately constant cross-sectional area in three-dimensional RBCs, and a relatively large value of k_p is assumed, to represent that property. A_{ref} and l_0 are chosen so that cells develop non-circular shapes with area A_{ref} and perimeter nl_0. All parameter values are taken from[18]. (The values for μ_m and μ'_m are incorrectly stated in[18]. The actual values used there are as stated here.)

Balancing the tensions and moments at each node with the fluid forces impinging on the external elements and balancing all viscous forces at the central node yields a system of $2(n+1)$ linear equations in the nodal velocities $\boldsymbol{u}_i = (u_i,v_i)$ and $\boldsymbol{u}_0 = (u_0,v_0)$. This system includes unknown terms dependent on the surrounding flow [18]. For comparison, simulations were also made for rigid circular particles. The translational velocity $\boldsymbol{u}_r = (u_r,v_r)$ and angular velocity ω_r are determined by requiring zero total force and moment on the particle.

The plasma is assumed to be a viscous, incompressible fluid governed by the Stokes equations. The equation for conservation of momentum is

$$\nabla\cdot\sigma = 0; \quad \sigma = \mu\left(\nabla u + \nabla u^T\right) - pI. \tag{5}$$

Here p is the pressure, $\boldsymbol{u}$ is the velocity, $\boldsymbol{\sigma}$ is the stress tensor, and $\mu = 10^{-2}$ dyn s/cm^2 is the viscosity. The incompressibility condition is replaced by the equation

$$\nabla^2 p = K\nabla\cdot u. \tag{6}$$

Using the stiffness parameter $K = 100$ ensures that $\nabla\cdot\mathbf{u} \approx 0$[18].

The velocity of a point on an external element of a flexible particle is assumed to be given by linear interpolation between the nodal velocities at the ends of the element. The velocities on rigid particles are given by $\boldsymbol{u}_{edge} = \boldsymbol{u}_r + \omega_r R\boldsymbol{t}$ where $\boldsymbol{t}$ is the vector tangential to the edge and R is the radius of the circular-particle. These velocities must match the adjacent fluid velocity (no-slip condition).

Fig. 2a shows an example of vessel bifurcation geometry. At the entrance to the mother vessel, constant pressure and Neumann conditions for $\boldsymbol{u}$ are specified. At exits of the daughter branches, the gradients of p and the values of $\boldsymbol{u}$ are prescribed, corresponding to Poiseuille flow with the specified flow rates. The fraction of bulk blood flow into daughter branch 1 is $\psi_1 = Q_1/Q_0$. The effect on flow rate of a RBC blocking a daughter vessel is assumed negligible, as the flow resistance created by a single cell in the daughter branch is small compared to the total resistance of the vessel downstream of the bifurcation. On the vessel wall, Neumann conditions for p and no-slip conditions for $\boldsymbol{u}$ are imposed. The main geometric and flow parameters are indicated in Figure 2(a). The radii of the circular arcs that link the vessel walls in the bifurcation are set to $r_1 = r_2 = r_0 = 3\ \mu$m. The length of each vessel is $Lv_0 = Lv_1 = Lv_2 = 5w_0/2$, unless otherwise stated. The branching angles are β_1 and β_2. The ratio of daughter vessel diameters is $r_d = w_1/w_2$.

The dependence of RBC distribution on vessel size (w_0), bulk blood distribution (ψ_1), and vessel geometry (β_1, β_2, and r_d) was investigated by varying these parameters. Arteriolar vessel diameters have been shown[10] to approximately follow the relationship $w_0^3 = w_1^3 + w_2^3$ at bifurcations. For given w_0 and r_d, this relationship determines the daughter vessel diameters. The total flow rate is assumed to be $Q_0 = 125 w_0^2\ \mathrm{s}^{-1}$, giving a mean flow velocity of 1 mm/s in an 8-μm mother vessel.

Unless otherwise specified, particle positions are initialized by setting $x_0 = -(15/8)w_0$. The initial y-coordinate y_0 is selected from the interval $[y_b, y_t]$ where $y_t = w_0/2 - R - w_{CFL} = -y_b$, to ensure that all points on the initial particle are at least a distance w_{CFL} from the vessel wall, representing a cell-free layer. For flexible cells, a circle with center at (x_0, y_0) and initial radius $R = 2.66\ \mu$m is discretized into n evenly spaced external nodes and one central node. This initial circular configuration is chosen to avoid biasing of the cell trajectory that might be caused by non-circular initial configurations. Rigid particles are modeled as smooth circles of radius $R = 2.66\ \mu$m with centers at (x_0, y_0).

Given a particular vessel geometry (i.e., w_0, β_1, β_2, and r_d), boundary conditions (determined by the flow fraction ψ_1), and the initial configuration of nodes representing the particle, a finite element solver is used to obtain the instantaneous velocities of the cell. The time-discretization employed is an explicit trapezoidal method of order 2. This solver is used to advance the nodal positions in time until either the cell is inside one of the daughter branches or the cell is within $0.1\ \mu$m of the far wall of the bifurcation and all its nodal velocities point towards the same daughter branch. A particle is considered to have entered the daughter branch if one of these conditions is satisfied. Further details on the numerical aspects are given in the Appendix.

The path of the particle's center of mass is defined as its particle streamline. For given vessel geometry and ψ_1, a separating particle streamline, starting at $y_0 = y_c(\psi_1)$, separates particle streamlines that enter branch 1 from those that enter branch 2. If all such streamlines starting with y_0 in the interval $[y_b, y_t]$ enter one branch, the separating particle streamline is defined as the top or bottom such streamline. The separating particle streamline and the associated $y_c(\psi_1)$ are obtained within a tolerance $\varepsilon_{bisection} \approx 0.05 w_0$ using a bisection algorithm (see Appendix). The separating streamline of the underlying flow is also defined for each flow fraction.

The RBC flux into branch 1, as a fraction of the total RBC flux, is given by

$$\Phi_1(\Psi_1) = \frac{\int_{y_c(\Psi_1)}^{y_t} s(y)\, u_d(y)\, dy}{\int_{y_b}^{y_t} s(y)\, u_d(y)\, dy}. \tag{7}$$

Here $s(y)$ is the density distribution of cell centers as they pass $x = x_0$, assumed to be constant and $u_d(y)$ is the horizontal velocity distribution of the cell centers at x_0, approximated by a quartic function (see Appendix).

RESULTS

Symmetric Bifurcations

Fig. 3a shows results for a flexible particle in a symmetric bifurcation, with $\psi_1 = 0.25$, $Q_0 = 8$ $\mu m^2/s$, $w_0 = 8$ μm, $r_d = 1$, and $y_0 = 1.24$ μm. The cell first transforms from an initial circular shape into an asymmetric shape that resembles observed shapes[18]. On reaching the flow divider between the two branches, the cell is deformed into a sandbag-like shape, which straddles the flow divider. Fig. 3b shows a similar shape observed in vivo.

In Fig. 3c, flexible cell streamlines are compared with fluid streamlines from the underlying flow field for the same vessel geometry and ψ_1. Comparing the outermost flexible cell streamlines with the outermost fluid streamlines reveals cell migration: the flexible cell streamlines tend towards the center of the mother vessel, upstream of the bifurcation. Comparing the inner cell streamlines with the inner fluid streamlines in the bifurcation region reveals that the cell streamlines can differ significantly from fluid streamlines in that region. In fact, one cell streamline enters branch 1 while a fluid streamline, which lies on this cell streamline at one point very near the bifurcation, enters branch 2.

Figures 4a-c show the function $y_c(\Psi_1)$ that defines the location of the separating streamline for flexible cells, rigid particles and the underlying fluid flow, for vessel geometries with $w_0 = 8$ μm, 10.1 μm, and 12.7 μm. For $\Psi_1 < 0.5$, the region above the curves (enters branch 1) is larger for rigid particles than for flexible cells, indicating that rigid particles tend to enter the low flow branch more than their flexible counterparts. The deviation between separating streamlines for particles and fluid separating streamlines is larger for rigid particles than for flexible cells, indicating that rigid particles deviate more than flexible cells from underlying streamlines. As the vessel size increases, the differences between flexible cell, rigid particle, and fluid separating streamlines become less significant.

Estimates based on eq. (8) for the fractional RBC flux $\Phi_1(\Psi_1)$ are shown in Fig. 4d-f for rigid particles and flexible cells. In these plots, partition of red blood cells in proportion to flow rate would be represented by the diagonal line $\Phi_1 = \Psi_1$. Phase separation is more pronounced for flexible cells than for rigid particles. The predicted curves depend on the assumed values of the parameter w_{CFL}, representing the width of the cell free layer at the initial upstream position. This parameter cannot be directly estimated from experimental data. Here, the assumed values are $w_{CFL} = 0$, 0.1 and 0.3 μm for geometries with $w_0 = 8$, 10.0 and 12.80 μm. These values are chosen so that the value Ψ_1 at which particles can enter branch 1 approximately corresponds to experimental values estimated from the empirical function[14] extrapolated to zero hematocrit. With the assumed values of w_{CFL}, predicted curves are consistent with experimental data.

Asymmetric bifurcations

Figure 5 shows results for a flexible particle in a symmetric bifurcation and an asymmetric bifurcation in which the daughter branches have widths 7.27 and 5.04 μm , with a diameter ratio of 1.44 (as in Fig. 2b) for $w_0 = 8$ μm. The curves for the asymmetric case are shifted to the right, indicating an increased tendency to enter the smaller branch. Fig. 5c depicts the change in Φ_1, together with the estimate derived from empirical results[14], with qualitative agreement. The agreement is less close for larger vessel sizes (results not shown).

Fig. 6 shows results for a T bifurcation with equal daughter branch widths, as in Figure 2c, compared to the symmetric case. In figure 6a, the curve $y_c(\Psi_1)$ is shallower for the T-bifurcation than for the symmetric case, but does not show a significant lateral shift, as would be expected if cells preferentially entered one of the branches. The length of the straight portion of the mother vessel is shorter in the T-bifurcation (13.8 μm) than in the symmetric case (18.3 μm). To correct for the effect of this difference on upstream lateral migration, the initial coordinate in the T-bifurcation was shifted from $x_0 = -15$ μm to $x_0 = -20$ μm. In figure 6b, the resulting $y_c(\Psi_1)$ is compared with that for a symmetric bifurcation with $x_0 = -15$ μm. The results do not differ significantly.

DISCUSSION

Upstream hematocrit distribution

Partitioning of hematocrit in bifurcations depends on the upstream hematocrit distribution and the trajectories of individual RBCs. In this study, the upstream *y*-positions of cell centers approaching the bifurcation are assumed to be uniformly distributed in a region whose width is limited so that the distance of cell centers from the wall is at least the initial cell radius plus the width of an assumed cell free layer. In reality, the upstream hematocrit distribution is determined by several factors including the exclusion effect (centers of finite-size cells cannot reach the vessel wall), cell migration, cell-to-cell interactions, cell deformation, length of the mother vessel, and the presence of an endothelial surface layer or glycocalyx[16]. For any given hematocrit distribution, the partition function $\Phi_1(\Psi_1)$ can be deduced from $y_c(\Psi_1)$ using eq. (7).

Particle deviation from fluid streamlines

If particles are small relative to the dimensions of the flow field, their trajectories closely follow the streamlines of the underlying flow. At low concentrations, the partition between the daughter branches is then fully determined by the upstream concentration distribution and the streamlines of the underlying flow field. A uniform upstream distribution leads to proportional partition of particles and fluid, whereas a narrow distribution allows the higher-flow branch to intercept a disproportionately large share of the particles. Particles of finite size relative to the flow domain may, however, deviate significantly from streamlines, affecting their partition between the branches. In the present results, two main causes for such deviations are evident: cell migration and daughter vessel obstruction.

In dilute suspension, RBCs tend to migrate toward the center-line of the vessel[8,18]. By narrowing the upstream concentration distribution, this migration increases the tendency of RBCs to enter the high flow branch. However, daughter vessel obstruction produces the opposite tendency. The factors influencing motion of rigid or slightly deformable particles in bifurcations were previously discussed by Fung[6,7] in terms of distributions of shear and pressure forces acting on the particles. In the present case, in which the particles are highly deformable and the flow rates in the branches are held constant, the particle motion can more easily be understood by considering its position relative to the underlying flow field. Since the separating fluid streamline is closer to the low-flow branch than to the high-flow branch, a RBC entering the bifurcation region on this streamline intercepts a relatively large part of the flow entering the low-flow branch. If the part of the cell in the low-flow branch lags the mean flow velocity in that branch, continuity of flow requires increased fluid velocity in the small remaining gap between the cell and the wall, generating a pressure difference across the cell that tends to drag it into that branch. Conversely, the cell intercepts only a small part of the flow entering the high-flow branch, and so the pressure difference generated across that part of the cell is less sensitive to a discrepancy between the cell and mean flow velocities. The net effect of daughter vessel obstruction is thus a tendency for the cell to enter the low-flow branch.

Effects of flexibility

Rigid circular particles do not experience lateral migration in unidirectional Stokes flow. Therefore, they are subject only to the obstruction effect, out of the two effects described. In bifurcations, they tend to enter the low-flow branch (Figure 4a-c) even when the corresponding fluid streamline enters the high-flow branch, and show a relatively weak phase separation effect (Figure 4d-f). Flexible cells, however, migrate towards the centerline. They make smaller obstructions than rigid particles because they tend to flatten against the flow divider. In the smallest geometry considered, the effect of migration exceeds the obstruction effect, and cells may enter high flow branches even when their underlying fluid streamlines enter low flow branches. As vessel size increases, the trajectories of flexible cells tend towards those of rigid particles, because the flexible cells deform less and because the effects of obstruction diminish as cell size becomes smaller relative to the vessel size. In each case, however, flexible cells still experience more nonuniform partitioning than rigid particles.

Effects of asymmetry

If the daughter vessels are of different sizes, particles show an increased tendency to enter the smaller branch (Figure 5). Since the cell's size causes a larger relative obstruction in the smaller branch, cells more likely to be drawn into that branch. The results for asymmetric branching angles (Figure 6) indicate that such asymmetry has little effect on the partition of hematocrit. Inertial effects are absent in Stokes flow, and there is no *a priori* reason to expect that cells would tend to follow one or other branch. Figure 7 shows shapes of deformed cells within the T bifurcation. Some asymmetry in shape is evident as the cell approaches the flow divider, but this does not lead to significant asymmetry in the $y_c(\Psi_1)$ curves.

Comparison with experimental data

Computed cell shapes in bifurcations show qualitative similarity with cell shapes observed in microvascular bifurcations, as for example shown in Figure 3b. The model results are consistent with experimental findings on hematocrit partition in bifurcations[14]. The extent of phase separation, as indicated by the difference between the function $\Phi_1(\Psi_1)$ and the line $\Phi_1 = \Psi_1$, decreases with increasing parent vessel size. In the case of different daughter vessel diameters, cells tend to enter the smaller branch. Branching angle has little effect. The Φ_1 - Ψ_1 relationships obtained show similar trends to those obtained experimentally, as shown in Figure 4. However, a direct quantitative comparison is not possible because of the unknown upstream hematocrit distribution *in vivo*.

Model limitations

A two-dimensional model is used to simulate RBC motion and deformation. While this model has been developed to reproduce observed three-dimensional behaviors as closely as possible[18], it has inevitable limitations. Some relevant quantities scale differently with mother vessel radius. For instance, the size of the relative obstruction scales as the inverse square of the daughter vessel radii in three dimensions but as the inverse in two dimensions. The obstruction effect may therefore be exaggerated in this model.

The results reported here neglect cell-to-cell interactions, and correspond to a low hematocrit. Under these conditions, RBCs migrate toward the center-line, and the upstream distribution of cells depends on the initial conditions and distance traveled (as in Figure 6). At finite hematocrits, cell-to-cell interactions oppose this migration, and broaden the hematocrit distribution. Pries et al.[11] showed that the phase separation effect decreased with increasing hematocrit. The method described here is suitable for the simulating the motion of multiple interacting RBCs in bifurcations, and also for predicting the effects of the endothelial surface layer[16] that is present *in vivo*.

Summary

To a first approximation, RBCs follow underlying fluid streamlines in bifurcations, but significant deviations from those streamlines can occur because of cell migration and obstruction effects. Cell migration tends to increase the fraction of cells entering high flow branches whereas cell obstruction of daughter vessel entryways has the opposite effect. These results show that the mechanical properties of red blood cells influence the hematocrit distribution in microvascular networks, and thereby affect physiologically relevant parameters including mean intravascular hematocrit[12] and RBC transit time through vascular beds.

ACKNOWLEDGMENTS

This work was supported by NIH grants HL034555 and HL07249, DOE Grant DEFG0202ER25533, NSF Grant DMS-0602173 (VIGRE) and the ARCS Foundation.

APPENDIX

Finite elements are used to express equations (5-6) as a system of linear equations. This system is coupled with the $2(n+1)$ equations arising from the force and moment balances for each node and the appropriate boundary conditions. The coupled linear system is solved to obtain the instantaneous velocities of the nodes on the cell. The finite element package FlexPDE (version 5.0.19) was used. In the simulations, the RBC membrane is discretized using $n = 20$ nodes. Between 100 and 400 fluid elements are used. The finite element package uses adaptive meshing to resolve narrow gaps between cells and walls, according to a user-specified tolerance. On a 1.66 GHz processor machine, computing the instantaneous velocities takes 10-20s.

Given cell nodal positions at time t^n, the nodal positions at some subsequent time $t^{n+1} = t^n + dt$ are found using an explicit trapezoidal, order-2 method[1]. In this scheme, the instantaneous velocities, u_i^n, are obtained using the finite element package (superscript corresponds to time t^n). The nodal positions at time t^{n+1} are predicted using a forward Euler estimate:

$$\tilde{x}_i^{n+1} = x_i^n + dt u_i^n; \quad 0 \le i \le n. \tag{8a}$$

These new nodal positions are used to obtain the instantaneous velocities $\tilde{u}_i^{n+1}$ of the cell nodes at time t^{n+1}. The final estimates of the nodal positions at time t^{n+1} are given by:

$$x_i^{n+1} = x_i^n + (dt/2)\left(u_i^n + \tilde{u}_i^{n+1}\right); \quad 0 \le i \le n. \tag{8b}$$

A time step of 1 ms was found to give numerical stability as well as good convergence, whereas the forward Euler method required a time step of around 0.2 ms for convergence. Generating a cell trajectory with the given method and time step usually takes 10-40 min on a 1.66 GHz processor machine.

To find y_c for a given vessel geometry and Ψ_1 using a bisection algorithm, quantities y_{below} and y_{above} are found such that y_c is in the interval $[y_{below}, y_{above}]$. The particle trajectory for $(y_{below}+y_{above})/2$ is then found, and the interval is halved, so that y_c is in the new interval. The algorithm is repeated until the size of the interval was less than $\varepsilon_{bisection} = 0.05 w_0$. The midpoint of this final interval is then used as an estimate for y_c; $\varepsilon_{bisection}$ can be viewed as an estimate of the error on this y_c. If a particle starting within .05 μm of either the top or bottom mother vessel wall enters branch 1 or branch 2 (respectively), all cells are presumed to enter only one branch and $y_c(\Psi_1)$ is taken as y_t or y_b, as appropriate.

To compute the upstream particle velocity profile, the instantaneous velocities of circular particles placed at nine locations across the channel are computed. The arithmetic average of the external node velocities is fitted with a quartic function ($r^2 > .98$) to obtain an estimate for $u_d(y)$, for use in eq. (7).

REFERENCES

1. Ascher, UM.; Petzold, LR. Computer Methods for Ordinary Differential Equations and Differential-Algebraic Equations. Society for Industrial and Applied Mathematics; Philadelphia: 1998. p. 73-82.
2. Audet DM, Olbricht WL. The motion of model cells at capillary bifurcations. Microvasc.Res 1987;33:377–396. [PubMed: 3613985]
3. El-Kareh AW, Secomb TW. A model for red blood cell motion in bifurcating microvessels. International Journal of Multiphase Flow 2000;26:1545–1564.
4. Enden G, Popel AS. A numerical study of the shape of the surface separating flow into branches in microvascular bifurcations. J.Biomech.Eng 1992;114:398–405. [PubMed: 1522734]
5. Enden G, Popel AS. A numerical study of plasma skimming in small vascular bifurcations. J.Biomech.Eng 1994;116:79–88. [PubMed: 8189718]
6. Fung YC. Stochastic flow in capillary blood vessels. Microvasc.Res 1973;5:34–48. [PubMed: 4684755]
7. Fung, YC. Biodynamics: Circulation: Chapter 5: Microcirculation. Springer-verlag; New York: 1984. The Velocity-Hematocrit Relationship; p. 241-249.
8. Goldsmith HL. Red cell motions and wall interactions in tube flow. Fed.Proc 1971;30:1578–1590. [PubMed: 5119364]
9. Leal LG. Particle Motions in A Viscous-Fluid. Annual Review of Fluid Mechanics 1980;12:435–476.
10. Mayrovitz HN, Roy J. Microvascular blood flow: evidence indicating a cubic dependence on arteriolar diameter. Am.J.Physiol 1983;245:H1031–H1038. [PubMed: 6660303]
11. Pries AR, Ley K, Claassen M, Gaehtgens P. Red cell distribution at microvascular bifurcations. Microvasc.Res 1989;38:81–101. [PubMed: 2761434]
12. Pries AR, Ley K, Gaehtgens P. Generalization of the Fahraeus principle for microvessel networks. Am.J.Physiol 1986;251:H1324–H1332. [PubMed: 3789184]
13. Pries, AR.; Secomb, TW. Blood Flow in Microvascular Networks. In: Tuma, RF.; Ley, K.; Duran, WN., editors. Handbook of Physiology: Section 2: The Cardiovascular System, Vol. 4. Microcirculation. 2008. In Press
14. Pries AR, Secomb TW. Microvascular blood viscosity in vivo and the endothelial surface layer. Am J Physiol Heart Circ Physiol 2005;289:H2657–H2664. [PubMed: 16040719]
15. Pries AR, Secomb TW, Gaehtgens P. Biophysical aspects of blood flow in the microvasculature. Cardiovasc.Res 1996;32:654–667. [PubMed: 8915184]
16. Pries AR, Secomb TW, Gaehtgens P. The endothelial surface layer. Pflugers Arch 2000;440:653–666. [PubMed: 11007304]
17. Schmid-Schonbein GW, Skalak R, Usami S, Chien S. Cell distribution in capillary networks. Microvasc.Res 1980;19:18–44. [PubMed: 7360046]
18. Secomb TW, Styp-Rekowska B, Pries AR. Two-dimensional simulation of red blood cell deformation and lateral migration in microvessels. Ann.Biomed.Eng 2007;35:755–765. [PubMed: 17380392]

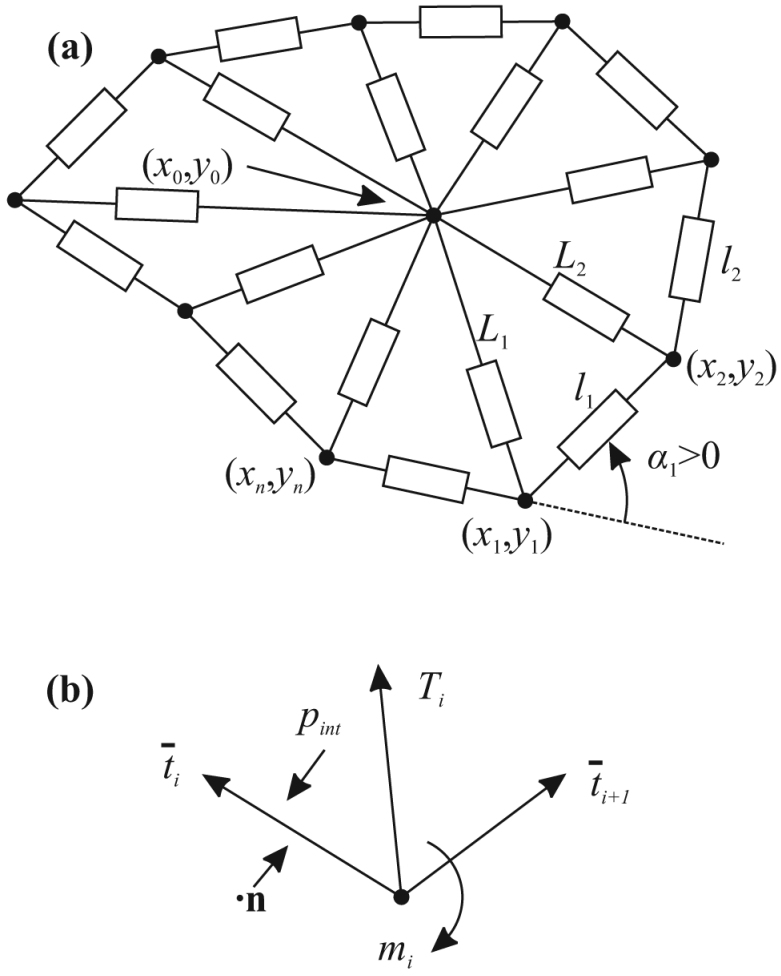

Figure 1.
(a) Schematic view of the two-dimensional model for a RBC. Rectangles denote viscoelastic/viscous elements of variable length, connected at the nodes. (b) Stresses and moments acting on node *i*.

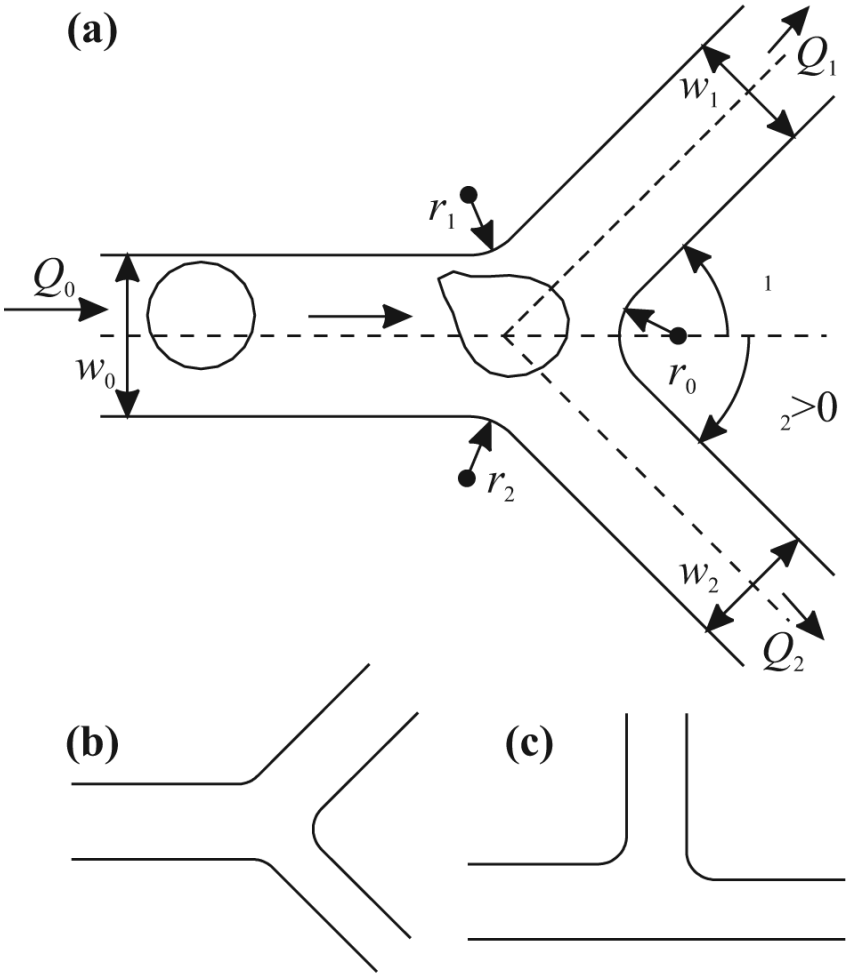

Figure 2.
Bifurcation geometries used. (a) Symmetric bifurcation with $\beta_1 = \beta_2 = \pi/4$ and $r_d = w_1/w_2 = 1$. (b) Bifurcation with asymmetric daughter vessel sizes; $\beta_1 = \beta_2 = \pi/4$ and $r_d = 3^{1/3} \approx 1.44$. (c) Bifurcation with asymmetric branching angles; $\beta_1 = \pi/2$, $\beta_2 = 0$, and $r_d = 1$.

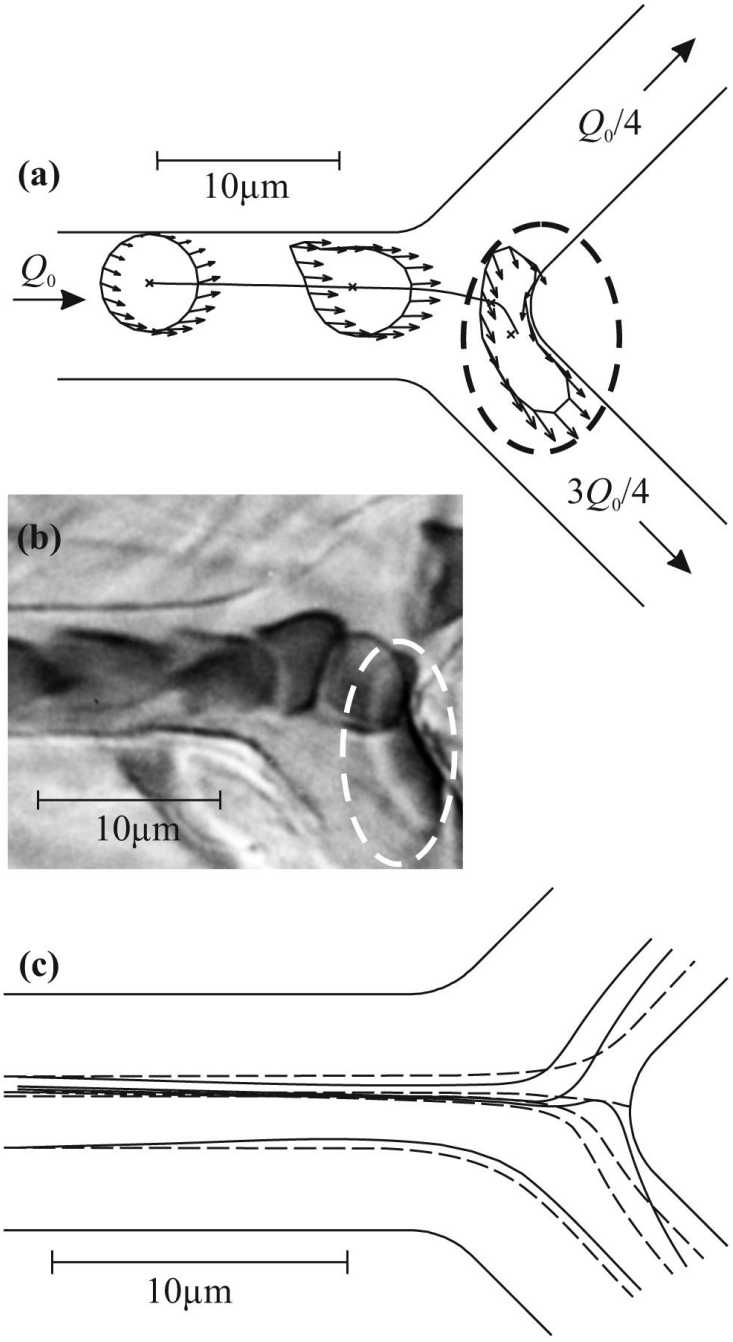

Figure 3.

(a) Example of center-of-mass trajectory, computed cell shapes and individual nodal velocities (arrows). Here Q_0 = 8 μm^2/ms, w_0 = 8 μm, ψ_1 = ¼. Cell shapes are shown at t = 0, 10, and 30 ms. Dashed ellipse indicates cell in sandbag-like shape, adjacent to the flow divider. (b) Photomicrograph of RBCs in a capillary bifurcation in the rat mesentery[13]. Scale is as in (a). One cell (indicated by dashed ellipse) is deformed into a sandbag-like shape, corresponding to the computed shape in (a). (c) Computed cell (solid) and underlying fluid (dashed) streamlines for the same geometry and ψ_1 = ¼. The dashed line that intersects the far wall of the bifurcation is the separating fluid streamline.

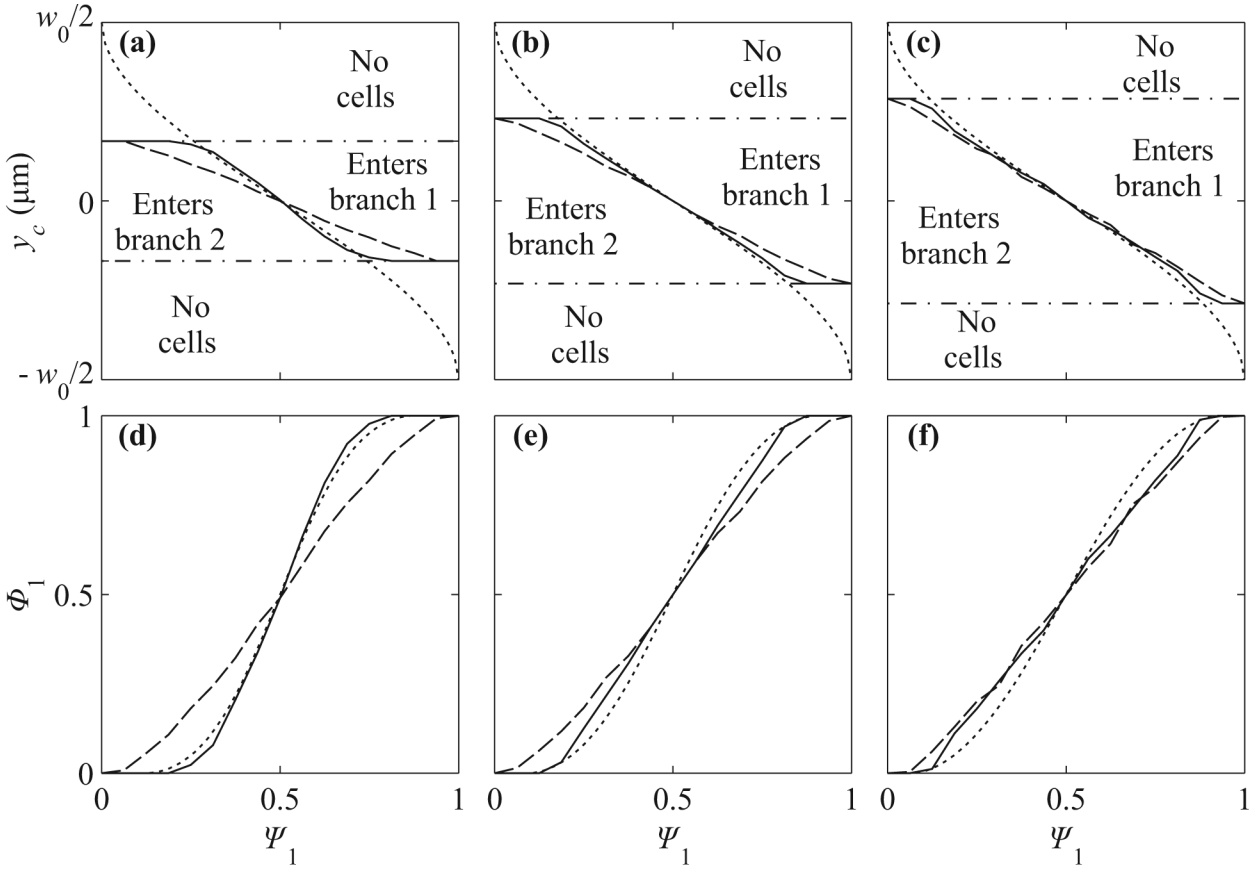

Figure 4.

Separating streamlines and partitioning in symmetric bifurcations. (a,d) w_0 = 8 μm. (b,e) w_0 = 10.08 μm. (c,f) w_0 = 12.80 μm. (a,b,c) Initial positions of cells corresponding to separating flexible cell streamlines (solid), initial positions corresponding to separating rigid particle streamlines (long dashed), and *y*-coordinate which the underlying separating fluid streamline (short dashed) passes through at $x = x_0$. (d,e,f) Estimates for fractional RBC flux, Φ_1, as a function of fractional blood flow rate, ψ_1. The cell-free layers used for the rigid particle (long dashed) and flexible cell (solid) estimates are *CFL* = 0, 0.1 and 0.3 μm in (d,e,f). Short dashed lines are experimental estimates from[14].

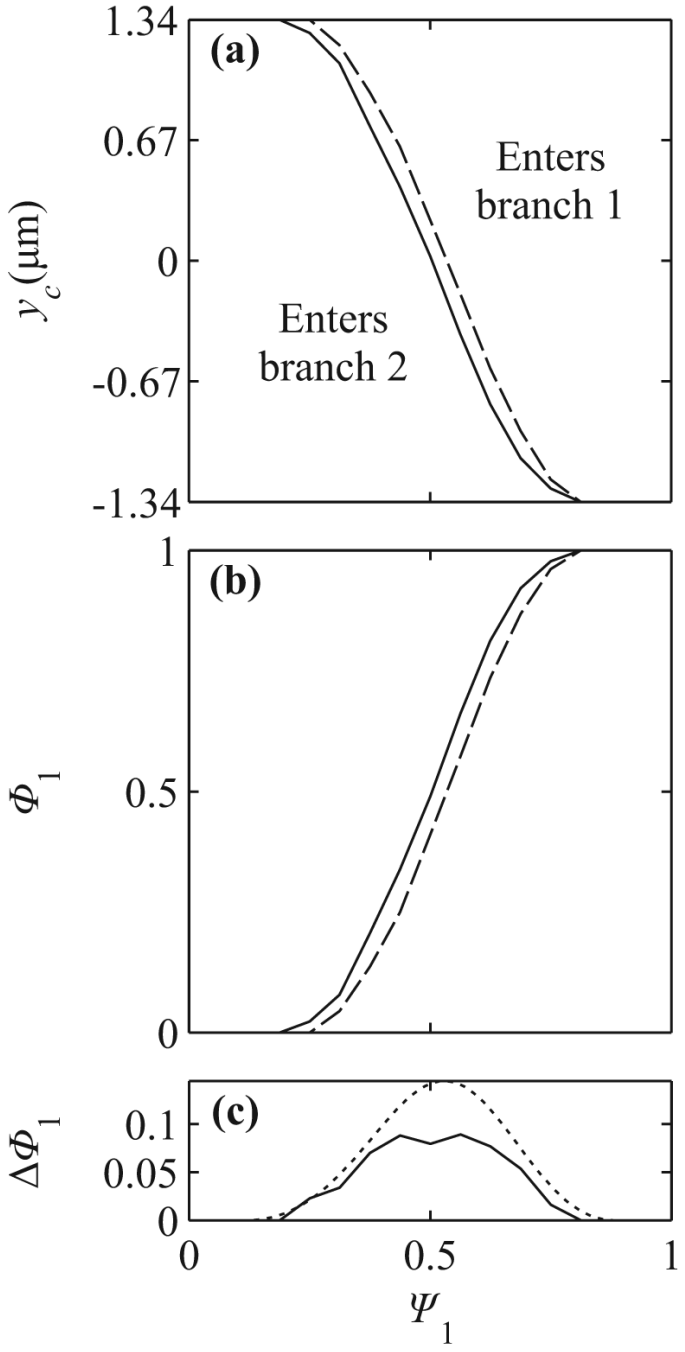

Figure 5.

(a) Comparison of results for symmetric bifurcations (solid) and bifurcations with asymmetric vessel diameters (dashed) for w_0 = 8 μm. Curves for the asymmetric bifurcation are shifted to the right. (b) Computed difference $\Delta\Phi_1$ between results for symmetric and asymmetric cases (solid curve) and estimated from empirical function[14] (dotted curve).

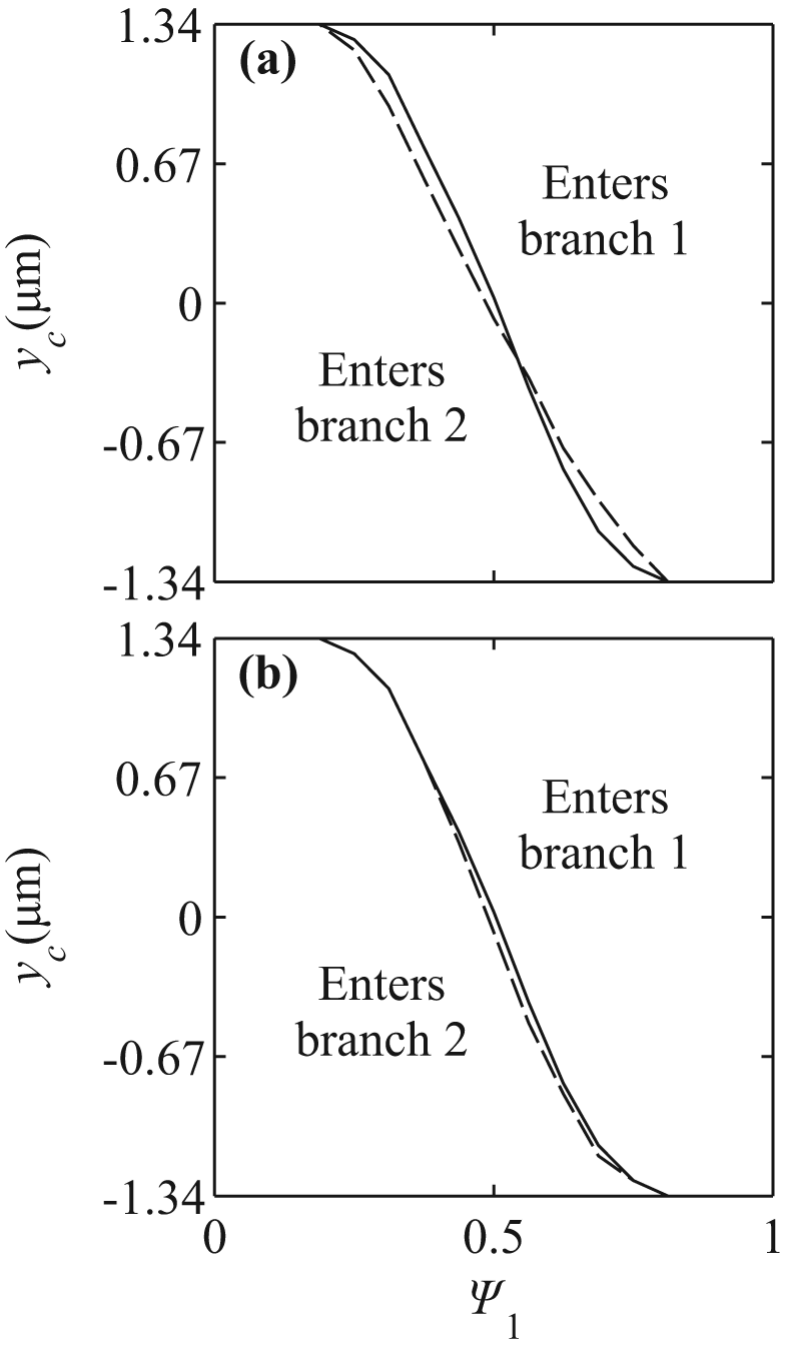

Figure 6.
Comparison of results from symmetric bifurcations (solid) with results from bifurcations with asymmetric branching angles (dashed). (a) Initial position $x_0 = -15$ μm. (b) Initial position $x_0 = -20$ μm in T-bifurcation, $x_0 = -15$ μm in symmetric bifurcation.

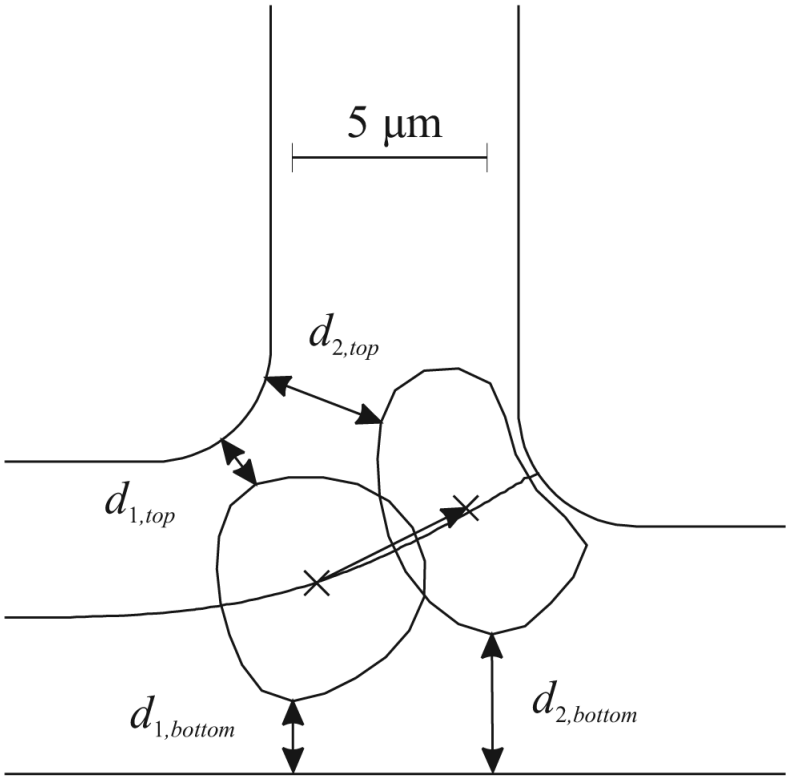

Figure 7.
Computed RBC shapes in a T-bifurcation, showing asymmetry of fluid streamline (solid line) and of gaps on either side of the RBC.